Shock and Static Pressure Demagnetization of Pyrrhotite and Implications for the Martian Crust

- Supplemental material -

Karin L. Louzada[1,2*], Sarah T. Stewart[2], Benjamin P. Weiss[3], Jérôme Gattacceca[4], Natalia S. Bezaeva[5]

[1]Netherlands Office for Science and Technology, Royal Netherlands Embassy, 4200 Linnean Avenue, NW, Washington, D.C. 20008, USA
[2]Department of Earth and Planetary Sciences, Harvard University, 20 Oxford Street, Cambridge, MA 02138, USA
[3]Department of Earth, Atmospheric and Planetary Sciences, Massachusetts Institute of Technology 54-814, 77 Massachusetts Avenue, Cambridge, MA 02139, USA
[4]Department of Geophysics and Planetology, CEREGE (CNRS, Aix-Marseille University), BP 80, 13545 Aix en Provence Cedex 4, France
[5]Earth Physics Department, Faculty of Physics, M.V. Lomonosov Moscow State University, Leninskie gory, 119991, Moscow, Russia

*louzada@post.harvard.edu

Contents:

		Figure	*Table*	*Page*
1.	X-ray diffraction	Figure S1	Table S1	2
2.	Chemical composition		Table S2	4
3.	Magnetic hysteresis		Table S3	5
4.	Anisotropy of magnetic susceptibility	Figure S2	Table S4	7
5	Experimental setup for shock experiments	Figure S3		9
6.	Pressure distribution in the shocked samples	Figure S4		10
7.	Impedance match solution		Table S5	11
8.	Hugoniot Elastic Limit	Figure S5	Table S6	12
9.	Photomicrographs of shocked pyrrhotite	Figure S6		14
10.	Domain interactions	Figure S7		15
11.	Magnetic imaging of pyrrhotite nodule	Figure S8		16
12.	References			17

Citation: Louzada, K.L., et al., Shock and static pressure demagnetization of pyrrhotite and implications for the Martian crust, Earth Planet. Sci. Lett. (2009), doi:10.1016/j.epsl.2009.12.006

1. X-ray diffraction

X-ray diffraction patterns were obtained for powdered samples using the Scintag XDS2000 fixed sample position powder diffractometer between 2 and 70° (2θ) at Harvard University. D-spacing values of peaks identified with known indices of pyrrhotite are shown in Table S1. Two additional weak peaks were detected at 2.8483 – 2.8643 Å and 1.5968 – 1.6096 Å, respectively. The latter peak could be related to the (312) plane in chalcopyrite ($CuFeS_2$), which may occur as small inclusions in natural pyrrhotite. However, Cu was not measured in the microprobe analyses (Table S2) and therefore this interpretation cannot be independently confirmed. Lattice parameters, *a* and *c*, were determined for a hexagonal lattice using the technique described in Nkoma and Ekosse (1999) and are consistent with previous pyrrhotite measurements (Dekkers, 1988; Nkoma and Ekosse, 1999). Monoclinic pyrrhotite was independently observed by a doublet at [208]. Thanks to W. Croft, Harvard University.

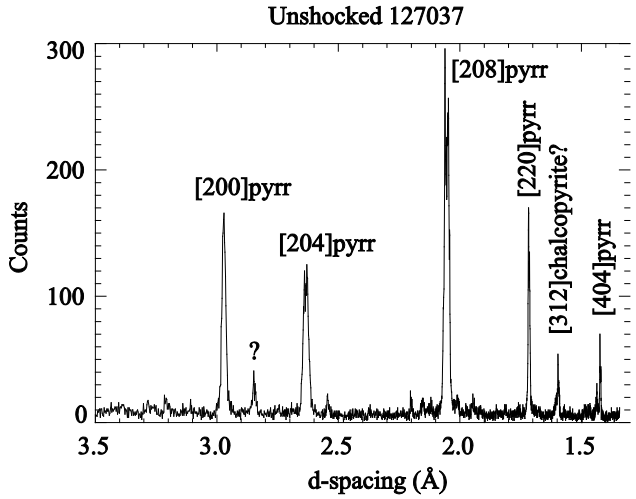

Figure S1 Example X-ray diffraction pattern for unshocked polycrystalline pyrrhotite.

Table S1 X-ray diffraction results

d-spacing	*Unshocked*	
	Nodule (No. 98080)	*Polycrystalline (No. 127037)*
$d_{(200)}$ (Å)	2.9737 (0.0058) [a]	2.9703
$d_{(204)}$ (Å)	2.6421 (0.0025) [a]	2.6300
$d_{(208)}$ (Å)	2.0642 (0.0025) [a]	2.0615, 2.0473 [c]
$d_{(220)}$ (Å)	1.7184 (0.0021) [a]	1.7179
$d_{(404)}$ (Å)	1.4324 (0.0005) [b]	1.4238
a (Å)	6.875 (0.006)	6.846 (0.033)
c (Å)	22.89 (0.06)	22.84 (0.23)
	Postshock	
	Nodule (98080-1D) (5.67 GPa)	*Polycrystalline (127037-A) (6.92 GPa)*
$d_{(200)}$ (Å)	2.9839	2.9800
$d_{(204)}$ (Å)	2.6436	2.6436
$d_{(208)}$ (Å)	2.0669	2.0669
$d_{(220)}$ (Å)	1.7215	1.7227
$d_{(404)}$ (Å)	1.4304	
a (Å)	6.874 (0.028)	6.884 (0.005)
c (Å)	22.94 (0.12)	22.91 (0.06)

[a,b] Average of three [(a)], two [(b)] measurements. [c] Split peak indicative of monoclinic pyrrhoitte. 1σ errors are indicated in parentheses.

2. Chemical composition

Spot microprobe chemical composition analyses were performed using the Camica Electron Microprobe at Harvard University. Operating conditions were 15 keV and 30.17 nA, with a beam size of 8 μm. Thanks to David Lange, Harvard University.

Table S2 Averaged (1σ) atom percentage chemical composition of pyrrhotite samples

Element	*Nodule (No. 98080)*	*Polycrystalline (No. 127037)*
S	52.70 (0.34)	53.29 (0.18)
Fe	47.07 (0.23)	46.70 (0.17)
Mn	b.d.l.	b.d.l.
Co	0.056 (0.007)	0.022 (0.005)
Ni	0.226 (0.050)	b.d.l.
Zn	b.d.l.	b.d.l.
Total	100.13	100.17
Fe/S	0.893 (0.01)	0.876 (0.01)
Number of measurements	11	26

b.d.l. = below detection limit

3. Magnetic hysteresis

Unshocked pyrrhotite magnetic hysteresis measurements (Table S3) were preformed on the Micromag Vibrating Sample Magnetometer with ±1 T maximum field at CEREGE, France. Postshock pyrrhotite magnetic hysteresis measurements were preformed on the Micromag Vibrating Sample Magnetometer at the Institute for Rock Magnetism, University of Minnesota with maximum field ±1.8 T. Due to variable monoclinic to hexagonal pyrrhotite distributions in the samples and the small sample masses direct comparison of the saturation moment (M_s) and saturation remanence (M_{rs}) cannot be made between the unshocked and shocked samples in this table. However, M_{rs}/M_s comparisons are meaningful indicators of relative differences in grain size. Thanks to M. Jackson and J. Bowles at IRM, University of Minnesota.

Table S3 Magnetic hysteresis results

Hysteresis	*Unshocked*		
Parameter (1σ)	*Nodule (No. 98080)* [a]	*Polycrystalline (No. 127037)* [a]	*Schist* [b]
M_s (Am^2/kg)	1.130 (0.027) $\times10^{-3}$	1.405 (0.029) $\times10^{-2}$	9.14 (6.02) $\times10^{-2}$
M_{rs} (Am^2/kg)	5.644 (0.022) $\times10^{-4}$	2.089 (0.022) $\times10^{-3}$	4.48 (2.90) $\times10^{-2}$
M_{rs}/M_s	0.4991 (0.010)	0.1487 (0.004)	0.499 (0.028)
B_c (mT)	5.507 (0.449)	4.643 (0.028)	23.8 (5.9)
B_{cr} (mT)	5.481 (0.552)	7.001 (0.075)	31.3 (11.7)
B_{cr}/B_c	0.9941 (0.0224)	1.508 (0.012)	1.29 (0.12)
mass (mg)	9.7	11.2	173.2-364.7 (n=10)
Domain size	SD/SP	MD	PSD

	Postshock [c]							
	Nodule					*Polycrystalline*		
Parameter (RMSres/RMSdata)	*98080-1L (1.74 GPa)*	*98080-1K (2.81 GPa)*	*98080-1H (2.89 GPa)*	*98080-1A (3.3 GPa)*	*127037-G (0.99 GPa)*	*127037-D (5.67 GPa)*	*127037-L* [d] *(9.83 GPa)*	*127037-N* (9.83 GPa)*
M_s ($\times10^{-3}$ Am^2/kg)	0.705 (0.02)	1.415 (0.07)	2.777 (0.86)	0.9217 (0.06)	1.065 (0.12)	4.329 (0.39)		15.95 (0.79)
M_{rs} ($\times10^{-3}$ Am^2/kg)	0.374 (0.03)	0.720 (0.06)	1.186 (0.30)	0.4538 (0.05)	0.330 (0.04)	2.022 (0.22)		7.698 (0.54)
M_{rs}/M_s	0.454 (0.06)	0.4266 (0.05)	0.4634 (0.15)	0.4412 (0.07)	0.317 (0.08)	0.4635 (0.04)	0.5527 (0.10)	0.4722 (0.02)
B_c (mT)	8.816 (2.03)	18.37 (2.76)	15.26 (8.70)	9.739 (2.82)		24.08 (10.59)	18.65 (7.65)	46.11 (5.53)
mass (mg)	1.2	12.0	17.3	1.9	1.3	9.2	<0.6	1.8

M_s = saturation magnetization (corrected for paramagnetic contribution), M_{rs} = saturation remanence, B_c = coercivity, B_{cr} = coercivity of remanence.
[a] Average hysteresis parameters (1σ) of measurements made in three perpendicular orientations. [b] Hysteresis parameters reported in Gattacceca, et al. (2007). [c] Geometric mean ($\sqrt[3]{\kappa_1 \cdot \kappa_2 \cdot \kappa_3}$) of ellipsoids fit to the hysteresis parameters measured in 12 orientations, where κ_1, κ_2 and κ_3 are the principal axes of the fitted ellipsoid. [d] Uncertain mass. * Shock direction is parallel to the easy plane of magnetization.

4. Anisotropy of magnetic susceptibility

The anisotropy of magnetic susceptibility (AMS) of pure pyrrhotite is field dependent (e.g., Martín-Hernández, et al., 2008) and our measurements using a Geofyzika KLY-2 KappaBridge AC Susceptibility Bridge with ac fields of 300 A/m at 920 Hz yielded erroneous results. Therefore, we determined AMS from 27 hysteresis loops in 12 directions obtained on the Princeton Measurements Vibrating Sample Magnetometer at the Institute for Rock Magnetism, University of Minnesota, with maximum field ±1.8 T. Low field susceptibility was determined from linear slopes fit to the data between -2.5 and +2.5 mT. We then solved for the susceptibility ellipsoid using the method described in Jelínek (1973) and Coe (1966).

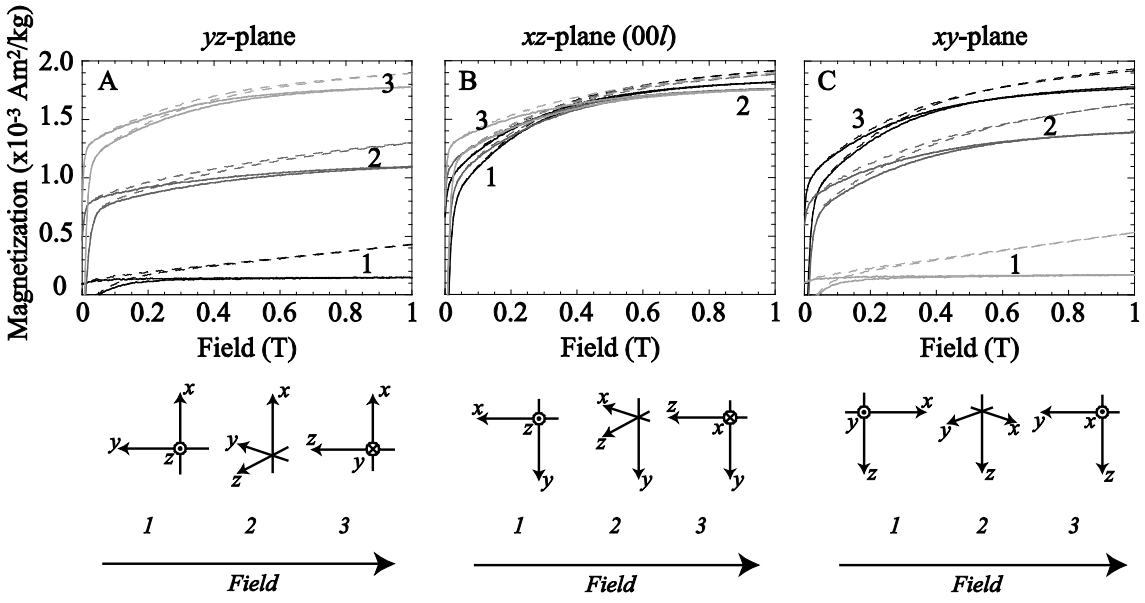

Figure S2 Partial hysteresis loops for the unshocked polycrystalline pyrrhotite (No. 127037) in three different orientations (1, 2 and 3). The inducing field is always oriented to the right and is confined to the *yz*-, *xz*- and *xy*-plane of the sample in panels **A**, **B** and **C**, respectively. (Right-handed coordinate system.) The *xz*-plane is parallel to the (00*l*) basal-plane. The oblate shape of the anisotropy is evident from the hysteresis loops in the *xz*-plane. Dashed lines are raw loops, solid lines are loops corrected for paramagnetic signal (linear fit between 1.5 and 1.6 T).

Table S4 Magnetic anisotropy results

AMS	*Unshocked*		
	Nodule (No. 98080)	*Polycrystalline (No. 127037)*	*Schist* [a]
P	45.98	56.24	1.741
L	29.97	2.202	1.087
F	1.534	25.53	1.601
P'	66.37	71.58	1.819
T	-0.776	0.608	0.697
RMS(res)/RMS(data)	0.25	0.03	

	Postshock							
	Nodule				*Polycrystalline*			
	98080-1L [a] *(1.74 GPa)*	*98080-1K (2.81 GPa)*	*98080-1H (2.89 GPa)*	*98080-1A (3.3 GPa)*	*127037-G (0.99 GPa)*	*127037-D (5.67 GPa)*	*127037-L (9.83 GPa)*	*127037-N* (9.83 GPa)*
P	21.96	22.79	5.448	46.46	64.38	253.9	14.20	60.62
L	17.12	4.684	2.410	5.285	1.505	1.375	8.626	1.181
F	1.211	4.865	2.260	8.791	42.77	1984.5	1.646	51.36
P'	31.87	22.79	5.450	46.98	98.62	501.5	16.78	104.2
T	-0.8757	0.0120	-0.0380	0.1325	0.803	0.884	-0.624	0.918
RMS(res)/RMS(data)	0.09	0.11	0.16	0.11	0.07	0.02	0.33	0.08

P = anisotropy degree (κ_1/κ_3), L = lineation (κ_1/κ_2), F = foliation (κ_2/κ_3), P' = corrected anisotropy degree ($P' = \exp\sqrt{\{2[(\eta_1-\eta)^2+(\eta_2-\eta)^2+(\eta_3-\eta)^2]\}}$, where $\eta_i = \ln(\kappa_i)$ and $\eta = (\eta_1+\eta_2+\eta_3)/3$), T = shape factor ($T = (2\eta_2-\eta_1-\eta_3)/(\eta_1-\eta_3)$). For a discussion on anisotropy see Jelínek (1981). [a] Measurement performed on the Geofyzika KLY-2 KappaBridge AC Susceptibility Bridge with ac field of 300 A/m and 920 Hz by M. Jackson and J. Bowles at IRM, UMN. * Shock direction is parallel to the easy plane of magnetization. [b] Low field susceptibility (±3 mT). RMS = root mean squared. The lower RMS (res)/RMS (data), the better the fit.

5. Experimental Setup Shock Experiments

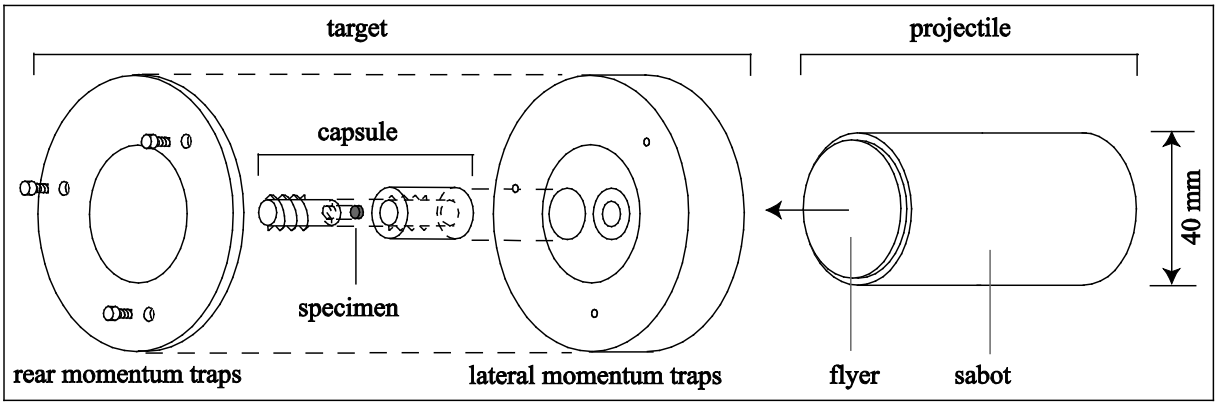

Figure S3 Example schematic diagram of an aluminum target configuration for a shock recovery experiment. Other configurations have a single capsule placed off-center. The inner capsule is smaller than the inner diameter of the 2G magnetometer. The disc-shaped specimens (3-12 mm diameter × <1 mm thick) are positioned approximately 1.5 mm from the impact surface. Self-shorting gauges attached to the impact side of the target assembly record the tilt of the projectile (generally <10 mrad). Redundant impact velocity measurements are performed by shorting pins and lasers placed in the path of the projectile prior to impact. The impact occurs in vacuum (<100 mtorr) at room temperature in the ambient magnetic field. The target assembly is decelerated and recovered downrange in a rag-filled catch tank.

6. Pressure distribution in the samples

Our CTH (McGlaun, et al., 1990) simulations of the shock experiments on pyrrhotite indicate that 74 and 94 vol% of the specimen experiences a maximum pressure within 0.5 GPa (13%) and 1.5 GPa (38%) of the calculated peak shock pressure, respectively.

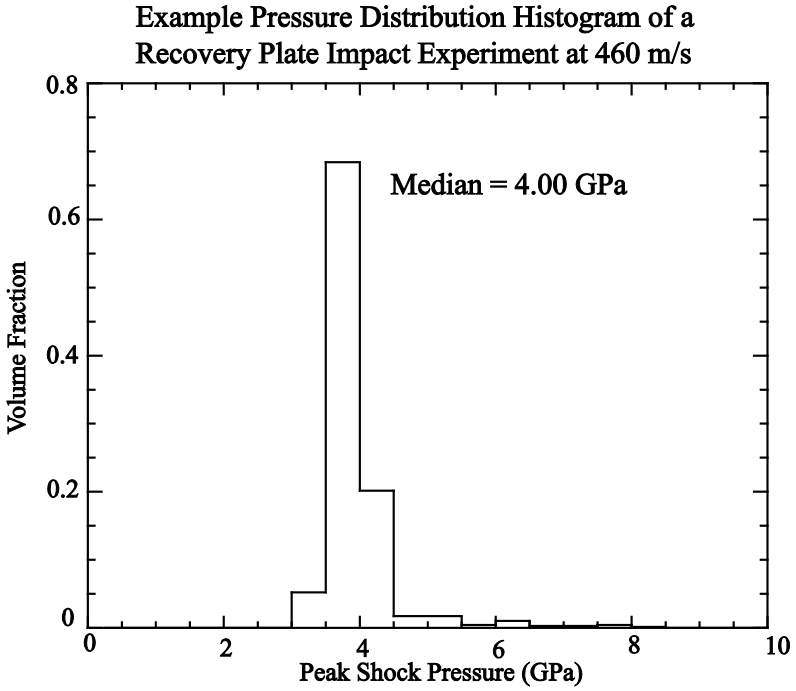

Figure S4 Histogram of the simulated pressure distribution as a function of sample volume in a pyrrhotite specimen at 460 m/s.

7. Impedance match solution

Principal stress in the shock experiments is determined using the impedance match solution, or planar impact approximation (e.g. Boslough and Asay, 1993; Melosh, 1989 p. 54-57), and the material shock parameters in Table S5. In the impedance match solution the impact is assumed to be between two infinite plates, reducing the problem to one dimension. At impact, the pressure in both the projectile (aluminum) and the target (specimen) must equal. Particle velocity and pressure (principal stress) are related to each other by the Hugoniot equation: $\sigma_1 = P_0 + \rho_0 U_S u_p$, where σ_1 is principal stress, P_0 is the initial pressure (~0), ρ_0 is the initial uncompressed density, and U_S and u_p are the shock and particle velocities in km/s, respectively. U_S and u_p are related to each other via the empirical relationship: $U_S = C + s \cdot u_p$, where C is the material specific bulk sound speed in km/s and s is the material specific dimensionless slope (Table S5). The planar impact approximation neglects attenuation of the shock wave and rarefactions that travel inward from the sides of the projectile. Errors in the shock pressure determination result from errors in the impact velocity measurement. Reflections from edge effects from the flyer will be slightly greater in the Wilson schist specimens as they are larger than the other specimens (12 mm, as opposed to 3 mm, in diameter). For the schist experiments we assume that the pressure in the specimen is equal to that in the aluminum, as their density and sound speeds are similar.

Table S5 Impedance match parameters

Material	*Uncompressed density* $(g/cm)^3$	*C* (km/s)	*S*	*Source*
Al-6061	2.703	5.33 (0.04)	1.34 (0.01)	fit to data between 0 and 3.8 km/s u_p (n = 105) (Marsh, 1980)
Al-2024	2.784 (0.008)	5.38 (0.02)	1.27 (0.02)	fit to data between 0 and 1.3 km/s u_p (n = 26) (Marsh, 1980)
Pyrrhotite	4.603 (0.003)	U_S = 4.543 (0.005) km/s		low pressure phase (elastic shock) weighted mean (n = 4) (Ahrens, 1979)
Schist	2.7515 (0.0255)	see Al-2024		mean (n = 4) (Table 2, main text)

1σ uncertainties are given in parentheses following mean values.

8. Hugoniot Elastic Limit

Two shock experiments to determine the Hugoniot Elastic Limit (HEL) of the solid polycrystalline pyrrhotite (No. 127037) were conducted in two perpendicular directions, parallel and perpendicular to the easy plane of magnetization (basal plane) at ~1150 m/s. Free surface velocities were determined simultaneously on the aluminum driver (1.2 mm thick) and a ~2 mm thick pyrrhotite specimen glued to the downrange side of the aluminum, using a Velocity Interferometer System for Any Reflector (Valyn-VISAR, Barker and Hollenbach, 1972). Shock velocity (U_s) in the pyrrhotite was determined from the break-out time difference of the VISAR traces on the driver and pyrrhotite sample (not shown). The experiment perpendicular to (00*l*) (solid line) shows a clear two wave structure with a plateau at ~300 m/s indicative of the elastic precursor. Based on CTH simulations, the pressure in the first wave (the HEL) is approximately 3.5 GPa, close to the pressure determined using the particle velocity doubling rule (~3 GPa; e.g., Boslough and Asay, 1993, p.32). Note that the peak measured particle velocity is approximately 50 m/s less than that predicted using the impedance match solution (Table S5). Velocity measurements parallel to (00*l*) (dashed line) do not show a clear two-wave structure.

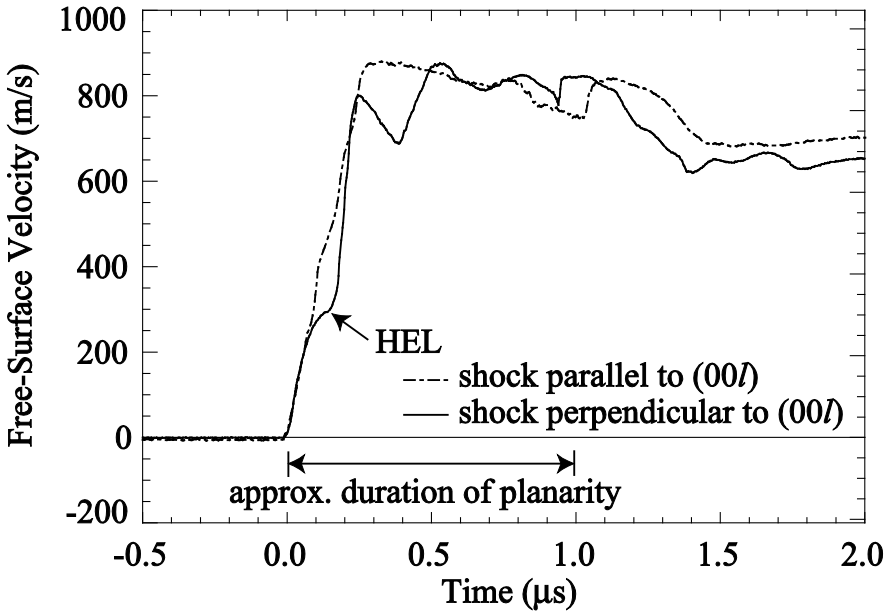

Figure S5 Free-surface laser velocity interferometry results for pyrrhotite specimens. Solid line = shock direction perpendicular to the basal plane of pyrrhotite (00*l*). Dashed line = shock direction parallel to (00*l*), indicated by * in other plots and tables throughout this work. HEL = Hugoniot Elastic Limit.

Table S6 Hugoniot experiment specifics

Specimen Name	*Specimen Mass* (g)	*Specimen thickness* (mm)	*Specimen density* (g/cm^3)	c_p (m/s)	c_s (m/s)	υ	v_i (m/s)	*Tilt* (mrad)	u_p (m/s)	σ_1 (GPa)	P (GPa)	U_s (km/s)	*HEL (GPa)*
12-C	2.147 (0.0017)	1.9228 (0.0062)	4.5724 (0.0173)	5.034 (0.082)	2.706 (0.025)	0.29	1156 (53.6)	0.36 (0.03)	505 (-24.3/+25.0)	10.8 (-0.53/+0.53)	6.54	-	
12-A*	1.786 (0.0017)	2.0984 (0.0072)	4.6074 (0.0081)	4.887 (0.059)	2.882 (0.021)	0.23	1171 (7.25)	3.77 (6.52)	511 (-2.4/+3.0)	10.9 (-0.08/+0.07)	5.80	4.81 (0.33)	~3.5

c_p and c_s = longitudinal and shear wave speeds. υ = Poisson's ratio. v_i = measured impact velocity. U_s = measured shock velocity. *HEL* = Hugoniot Elastic Limit. u_p = calculated particle velocity. σ_1 = calculated principal stress. P = calculated average pressure. 1σ uncertainties are given in parentheses following mean values.

9. Photomicrographs of shocked pyrrhotite

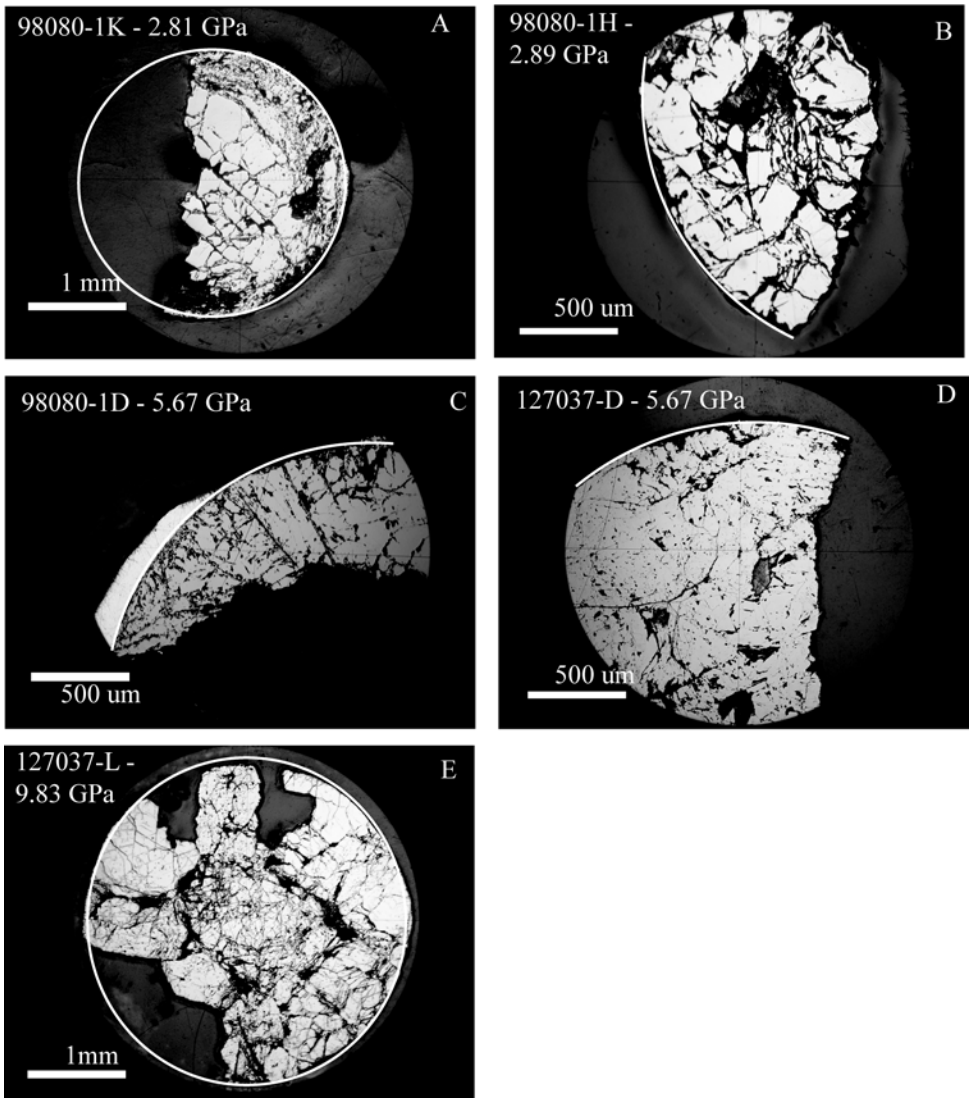

Figure S6 Photomicrographs of shocked and recovered pyrrhotite nodule (**A-C**) and single crystal (**D and E**) specimens. The white line indicates the original perimeter of the disc shaped specimen. The pressures in these samples were near enough to or above the Hugoniot Elastic Limit of pyrrhotite (~3 GPa) that fracturing may have occurred during compression. The nodule specimen shocked at 1.74-1.96 GPa (with uncertain pressure history) and one of the polycrystalline specimens shocked at 0.99 GPa were also broken when removed from their capsule. In these samples, tensile stresses may have exceeded the dynamic tensile strength of pyrrhotite (~100s of MPa in igneous rock, Ai and Ahrens, 2004) during release due to the fact that the wave front is not a perfect step function.

10. Domain interactions

Domain interactions can be analyzed using the technique described in (1958). Deviation from idealized noninteracting single domain assemblages with uniaxial anisotropy can be described by the differential remanence, $\Delta M(H)=M_{DC}(H)-[1-2M_{IRM}(H)]$, where $M_{IRM}(H)$ and $M_{DC}(H)$ are the normalized magnetic moments measured during acquisition of isothermal remanent magnetization and dc backfield demagnetization of saturation isothermal remanent magnetization in a field, H, respectively. Negative ΔM values result from negative interaction yielding a net demagnetizing effect (as is the case in multidomain grains) and positive ΔM values result from positive interactions, leading to stabilization of the magnetization. If shock induced magnetic hardening is a direct result of domain-size changes, then the new domains must not interact significantly.

In the MD polycrystalline pyrrhotite (grey lines, Figure S7), the differential remanence is negative at all fields. The minimum differential remanence at low-field is less in the postshock (9.83 GPa, triangles) case than it is in the unshocked (diamonds) case. Comparisons with Figure 3 of Wehland et al. (2005) indicate that the changes are consistent with a decrease in grain size (a decrease in the net demagnetizing effect), but that the interactions in the polycrystalline pyrrhotite are of multidomain type. The changes in domain interactions in the SD/DP nodule are much more subtle, both unshocked and shocked differential remanences are very small (negative) indicating that the nodule consists of nearly entirely noninteracting single-domains consistent with its uniaxial magnetic anisotropy (linear magnetic fabric).

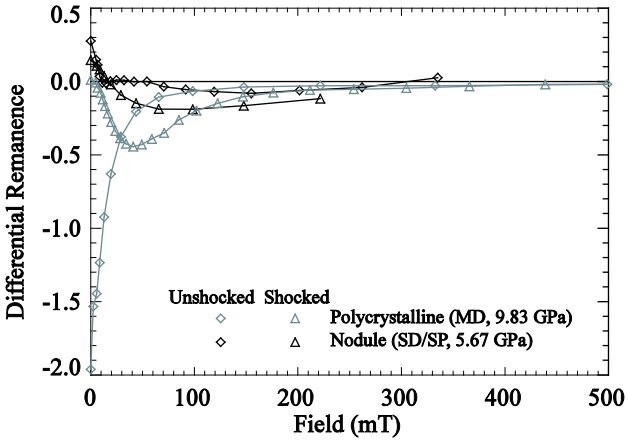

Figure S7 Differential remanence of unshocked (diamonds) and shocked (9.83 GPa) triangles MD single crystal pyrrhotite. Negative ΔM values indicate multidomain type interactions.

11. Magnetic imaging of the pyrrhotite nodule

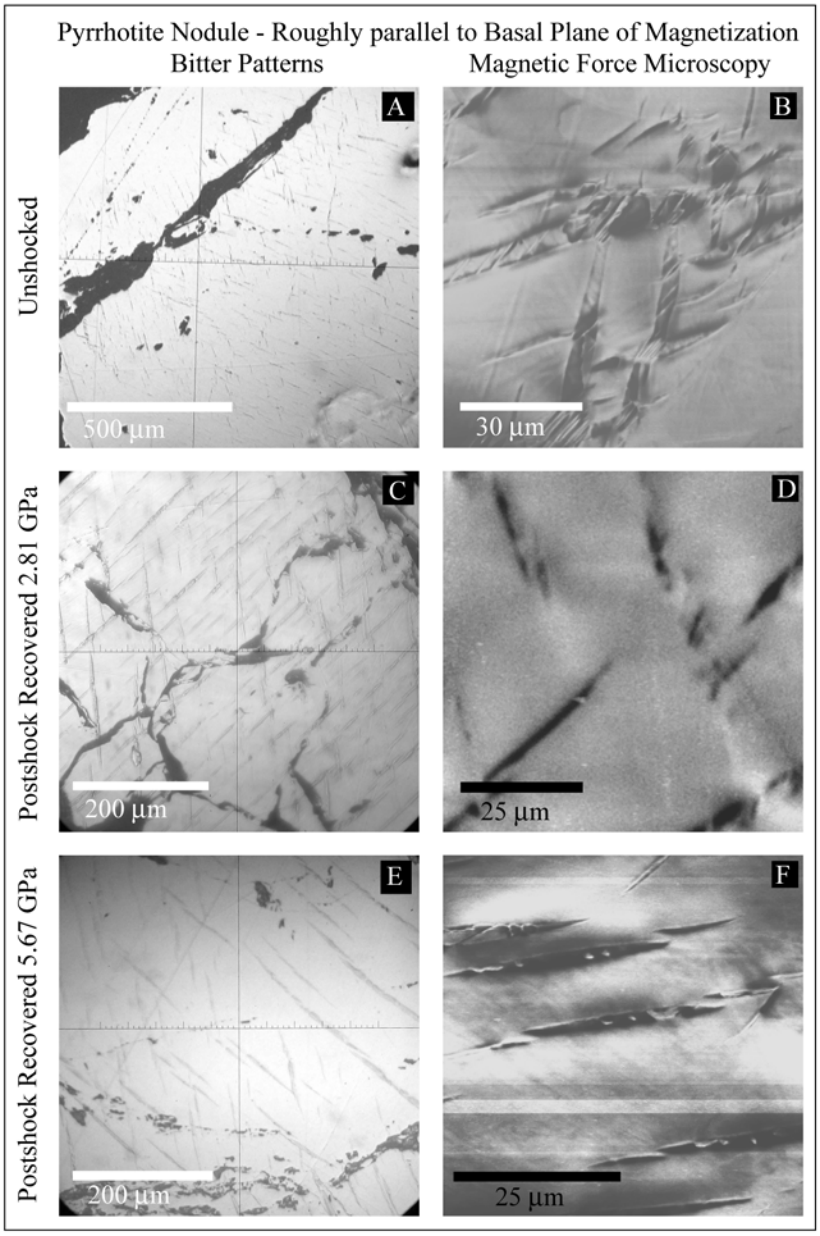

Figure S8 Magnetic imaging of polished (0.02 µm thick) (**A, B**) unshocked and (**C-F**) postshock recovered SD/SP pyrrhotite, with the shock direction roughly parallel to the basal plane for all samples. Postshock samples are AF demagnetized in 85 mT peak fields. Horizontal lines in (**F**) are an artifact of tracking error.

12. References

Ahrens, T.J., 1979. Equations of State of Iron Sulfide and Constraints on the Sulfur Content of the Earth. JGR 84, 985-998.

Ai, H.-A., Ahrens, T.J., 2004. Dynamic tensile strength of terrestrial rocks and application to impact cratering. MAPS 39 (2), 233-246.

Barker, L.M., Hollenbach, R.E., 1972. Laser interferometer for measuring high velocities of any reflecting surface. Journal of Applied Physics 43, 4669-4675.

Boslough, M.B., Asay, J.R., 1993. Chapter 2: Basic Principles of Shock Compression, in: Asay, J.R., M., S. (Eds), High-Pressure Shock Compression of Solids. Springer-Verlag, New Yok, pp. 7-42.

Coe, R.S., 1966. Analysis of Magnetic Shape Anisotropy Using Second-Rank Tensors. JGR 71 (10), 2637-2644.

Dekkers, M.J., 1988. Magnetic properties of natural pyrrhotite Part I: Behaviour of initial susceptibility and saturation-magnetization-related rock-magnetic parameters in a grain-size dependent framework. PEPI 52, 376-393.

Gattacceca, J., Lamali, A., Rochette, P., Boustie, M., Berthe, L., 2007. The effects of explosive-driven shocks on the natural remanent magnetization and the magnetic properties of rocks. PEPI 162, 85-98, doi:10.1016/j.pepi.2007.1003.1006.

Jelínek, V., 1973. Precision A.C. bridge set for measuring magnetic susceptibility of rocks and its anisotropy. Studia Geophysica & Geodaetica 17, 36-48, doi:10.1007/BF01614027.

Jelínek, V., 1981. Characterization of the magneitc fabric of rocks. Tectonophysics 79, T63-T67, doi:10.1016/0040-1951(81)90110-4.

Marsh, S.P., (Ed) LASL Shock Hugoniot Data, University of California Press, Berkeley, California, 1980, 658 pp.

Martín-Hernández, F., Dekkers, M.J., Bominaar-Silkens, I.M.A., Maan, J.C., 2008. Magnetic anisotropy behaviour of pyrrhotite as determined by low-and high-field experiments. GJI 174, 42-54, doi: 10.1111/j.1365-246X.2008.03793.x.

McGlaun, J.M., Thompson, S.L., Elrick, M.G., 1990. CTH: A 3-dimensional shock-wave physics code. Int. J. Impact Eng. 10, 351-360, doi:10.1016/0734-743X(90)90071-3.

Melosh, H.J., 1989. Impact Cratering: A Geologic Process, Oxford University Press, New York.

Nkoma, J.S., Ekosse, G., 1999. X-ray diffraction of chalcopyrite $CuFeS_2$, pentlandite $(Fe,Ni)_9S_8$ and pyrrhotite $Fe_{1-x}S$ obtained from Cu-Ni ore bodies. Journal of Physics: Condensed Matter 11, 121-128.

Wehland, F., Stancu, A., Rochette, P., Dekkers, M.J., Appel, E., 2005. Experimental evaluation of magnetic interaction in pyrrhotite bearing samples. PEPI 153, 181-190, doi:10.1016/j.pepi.2005.05.006.

Wohlfarth, E.P., 1958. Relations between different modes of the acquisition of the remanent magnetization of ferromagnetic particles. Journal of Applied Physics 29, 595-596.